Available online at www.sciencedirect.com

SCIENCE DIRECT®

Materials Chemistry and Physics 85 (2004) 113–119

MATERIALS CHEMISTRY AND PHYSICS

www.elsevier.com/locate/matchemphys

Structure of amorphous iron-based coatings processed by HVOF and APS thermally spraying

M. Cherigui, H.I. Feraoun, N.E. Feninehe*, H. Aourag, C. Coddet

LERMPS, UTBM, 90010 Belfort Cedex, France

Received 14 July 2003; received in revised form 7 December 2003; accepted 17 December 2003

Abstract

High-velocity oxy-fuel (HVOF) and air-plasma spraying (APS) were used to produce Fe_3Si and FeNb alloy coatings. Adjusting the spraying conditions, amorphous coatings were obtained from the FeNb powder. However, for the Fe_3Si powder, crystalline deposits were produced in all cases. Boron additives were used to improve the aptitude of the Fe_3Si alloy to form an amorphous phase. In this perspective, first-principle calculations were elaborated to investigate the electronic structure of crystalline FeNb and Fe_3Si. It was shown that the introduction of boron impurities into the alloy matrix lead to the lowering of the structural stability, and made its electronic density of state more comparable to the corresponding FeNb structure.

Keywords: Amorphous coatings; Thermal spraying; Magnetic properties; Fe_3Si; FeNb; Rapid quenching; Intermetallics; Electronic structures

1. Introduction

The development of amorphous and nanocrystalline materials has attracted significant interest in the field of new materials design. Indeed, the magnetic, chemical and mechanical properties of materials are largely enhanced when the size of crystallites becomes nanometric. In addition, the absence of crystal structure implicates a macroscopic behavior fairly different from that of corresponding to the polycrystalline state, especially, mechanical and magnetic properties.

Amorphous metallic materials can be obtained by rapid quenching [1] in order to prevent traditional solidification phenomena from occurring. Thus, one can obtain materials with a disordered structure beyond some interatomic distances. As a consequence, the microstructure does not contain grains as in polycrystals, and so no grain boundaries, elements that control to a large extent the macroscopic behavior. Accordingly, some amorphous metallic alloys exhibit exceptional mechanical, chemical and magnetic properties due to the lack of long-range order in their atomic arrangement [2]. However, industrial applications of these amorphous alloys have been restricted due to the difficulties encountered in the production of bulk quantities and the limitations in thickness caused by rapid quenching methods such as melt spinning [2]. There exists a large number of techniques to produce amorphous alloys other than rapid quenching, namely vapor condensation on cold substrate, cathode sputtering, ion bombardments, electrolysis, and amorphization methods in solid state [3]. Thermal spraying has become a very advantageous method owing to the high deposition rates and low operation costs involved [4,5]. The thermal spraying process permits the use of complex geometry substrates. Then its use is extended to a wide range of applications. Furthermore, free standing near net shape forms can also be produced by this droplet consolidation technique [6,7].

The interest found in Fe_3Si alloys was derived by the intriguing magnetic properties of this compound, specifically its magnetic susceptibility $\chi(T)$ which is small at low temperatures T, but grows rapidly until it peaks near 500 K and starts decreasing slowly above this value following the Curie–Weiss law. Benoit [8] proposed that the broad maximum susceptibility is due to an antiferromagnetic transition, but the results of subsequent neutron scattering [9] show that the lack of crystalline structure plays a key role in this special magnetic behavior.

In order to take advantage of these properties, amorphous Fe_3Si coatings were produced using thermal spraying. Subsequent trial tests with different spraying conditions were not successful for this alloy, whereas it has been easy to obtain amorphous FeNb coatings. Following several

---

* Corresponding author. Tel.: +33-3-84-58-31-16;
fax: +33-3-84-58-32-86.
E-mail address: nour-eddine.fenineche@utbm.fr (N.E. Feninehe).

0254-0584/$ – see front matter © 2004 Elsevier B.V. All rights reserved.
doi:10.1016/j.matchemphys.2003.12.017

Table 1
Spraying parameters

Parameters	Tube	Plate
Oxygen flow (l min^{-1})	420	420
Methane flow (l min^{-1})	140	140
Carrying N_2 (l min^{-1})	20	20
Feed rate (g min^{-1})	35	35
Spray distance (mm)	300	300
Plate speed (m s^{-1})		≈1

suggestions [1], some additive elements within the Fe_3Si matrix can lead to an easier amorphization. Looking into the literature, it was found that Fe_3Si–B amorphous ribbons have been widely used as a magnetic core material and there are also many reports on their crystallization behavior [10,11]. Consequently, a structural and electronic study of crystalline $Fe_{3-x}SiB_x$ and FeNb alloys were initiated via first-principle total-energy simulation method. The suppercell approach was used to examine the local effect of boron atoms in the Fe_3Si structure, and compare the appropriate

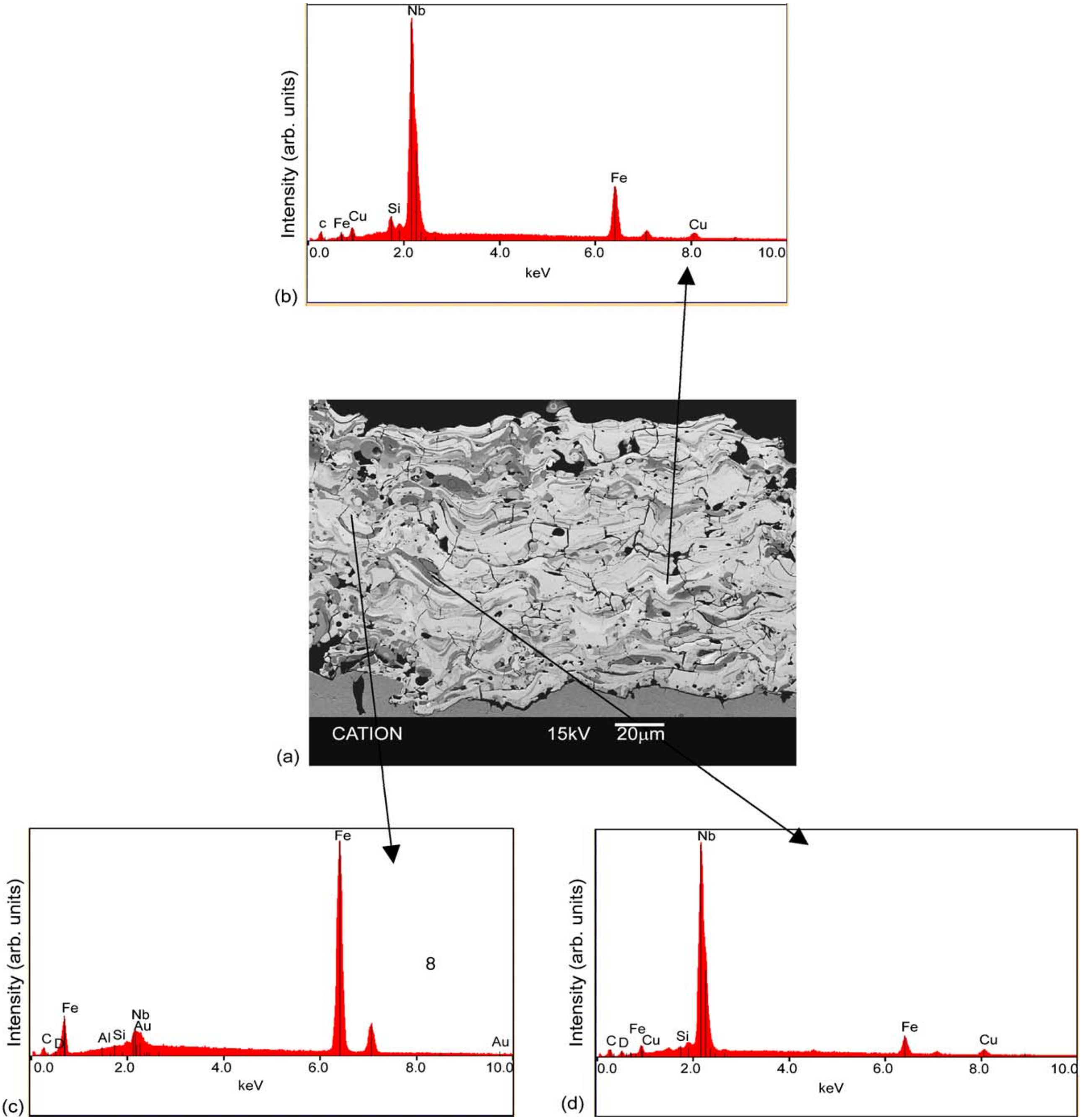

Fig. 1. Morphology and structure of FeNb coatings. (a) SEM image and EDS analysis of the white zone (b), the non-molten particles (c) and the gray zone (d).

properties to those of FeNb alloy. In this study, a FeNb alloy is used as a reference material since its amorphization was relatively easy as well as it was stated elsewhere [12].

2. Materials and experiments

High-velocity oxy-fuel (HVOF) and air-plasma spraying (APS) were used to spray Fe–50 wt.% Nb (0–44 μm) and Fe–6.5 wt.% Si (0–150 μm) particle powders. The copper substrate used is a 70 mm × 25 mm and 0.8 mm thick sheet fixed on a port sample moved at a velocity of 200 rpm. The spraying experimental conditions are given in Table 1. To avoid significant heating during the progress of the process, the substrate was cooled on its backside using compressed air. Several passes (15–25) of the torch were necessary to produce 200–300 μm thick coatings.

The as-sprayed coatings were cut and polished using standard procedures for thermal sprayed metal coatings. Optical microscopy was used to obtain low magnification images using a Nikon Epiphot 200 microscope. Scanning electron microscopy (SEM) was used to obtain clear images. The procedure adopted for image acquisition entailed a backscattered electron imaging mode for higher contrast between pores, oxide areas and metal matrix. Energy-dispersive spectrometry (EDS) analysis was employed while imaging on SEM to obtain the elemental composition at different areas of the coating cross-section. Starting powders were also investigated using X-ray diffraction (XRD). It was conducted using a PHILIPS X'PERT diffractometer at a scanning rate of 3° min^{-1} and with copper radiation (Cu Kα).

3. Experimental results

Figs. 1a and 2a are SEM images of FeNb and Fe_3Si coatings showing the typical aspect of the as-sprayed structure. The deposits were fairly dense and well-bonded on the copper substrate. The individual splats were clearly visible within the coatings. For a given coating, the morphology of these splats is well different from one area to the other, and this is true for both types of coatings. Some of them have melted and flowed extensively on impact whereas, for others, the particulate nature of the starting material was still clearly apparent.

In metallic coatings, it is difficult to identify whether the dark areas observed in the microstructure represent gas porosity, interlamellar pores or oxides. EDS analysis can be used to obtain the elemental composition from different areas. This analysis made it possible to detect the presence of two phases for the FeNb coating, one in white color (36.3% Fe and 63.2% Nb) and other in gray color (20.2% Fe and 78.8% Nb). For Fe_3Si coatings, the presence of Si with almost the same percentage as in the powder (78.3% Fe and 5.9% Si) can be noted. The presence of other elements like S, Cr, Pd and C in poor amounts was also observed.

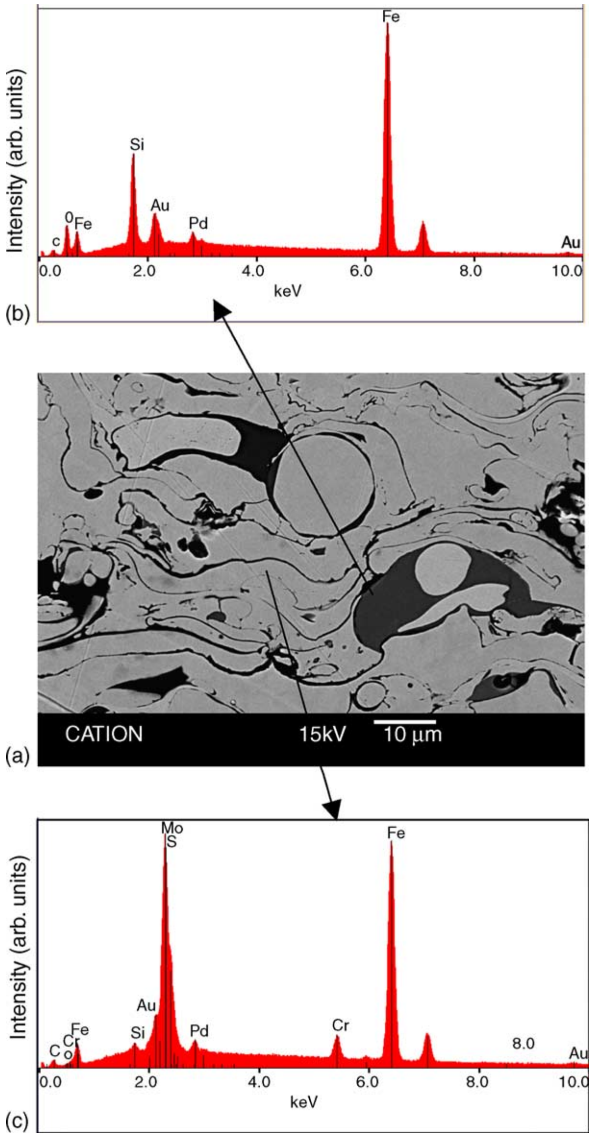

Fig. 2. Morphology and structure of Fe_3Si coatings. (a) SEM image and EDS analysis of the gray zone (b) and the white zone (c).

Image analysis was applied to these coatings produced by the APS process in order to quantify the content of porosity and oxides. For the Fe_3Si coatings, Fig. 2 shows a less dense deposit than the FeNb one. The porosity of the Fe_3Si coating is superior than that of FeNb: we have about 15 ± 2.5 and 9.5 ± 2% of porosity ratios, respectively. The presence of these various zones in the FeNb coatings suggests that the structure is completely different from a simple crystalline structure and XRD results confirmed these conclusions.

Fig. 3 illustrates XRD patterns for FeNb alloy. Regarding to the peak intensities and their broadening, we noticed a mixture of amorphous and extremely fine crystalline phase (nanocrystalline). This partially amorphous structure of FeNb type with the presence of NbO_2 and Nb_2O_5 oxides results from the use of the HVOF technique where the oxidation phenomena are significant. However, for Fe_3Si alloy, the X-ray characterization shows that the structure is

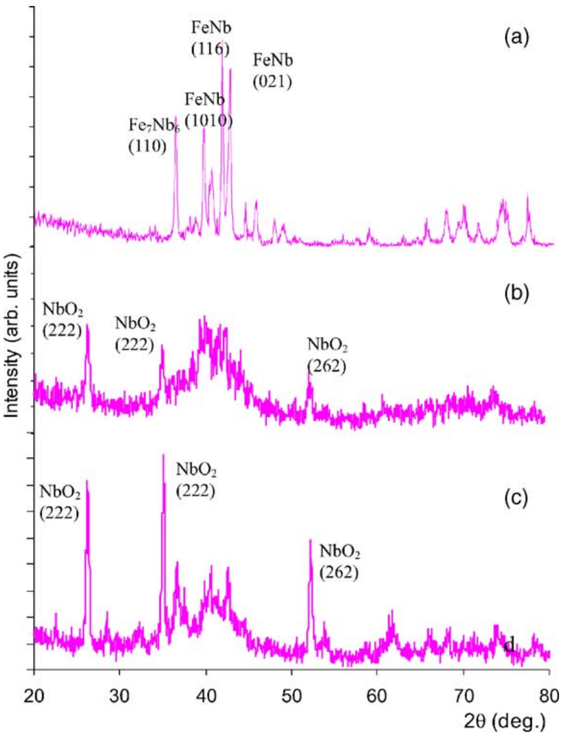

Fig. 3. X-ray diffraction patterns for (a) FeNb powder, (b) HVOF coatings and (c) APS coatings.

perfectly crystalline: the basically cubic structure α_1–Fe_3Si (DO_3), which is characteristic for the low-silicon content Fe_3Si alloys is predominant (Fig. 4). These results agree with those obtained by rapidly quenched $Fe_{100-x}Si_x$ alloy [13,14] and mechanically alloyed Fe_3Si [15].

Fig. 5 shows standard hysteresis loops for the Fe_3Si coatings. We can note that this Fe_3Si is a soft ferromagnet with an average coercivity H_c of 4, 6.7 and 8 Oe for powder, APS and HVOF coatings, respectively. On the other hand, the magnetic characterization shows the super paramagnetic state of the FeNb alloy coating.

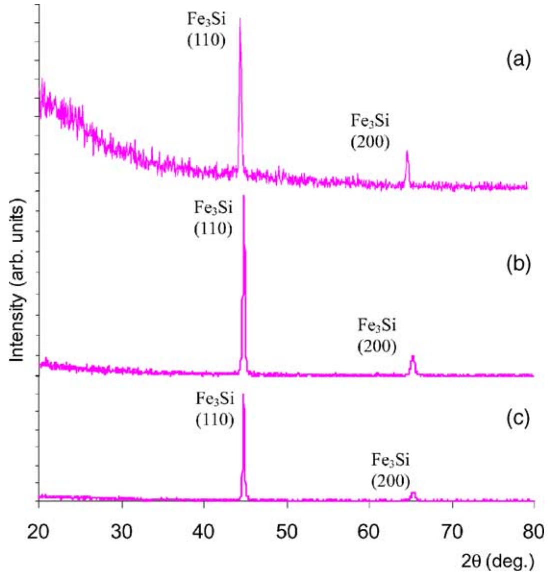

Fig. 4. X-ray diffraction patterns for (a) Fe_3Si powder, (b) HVOF coatings and (c) APS coatings.

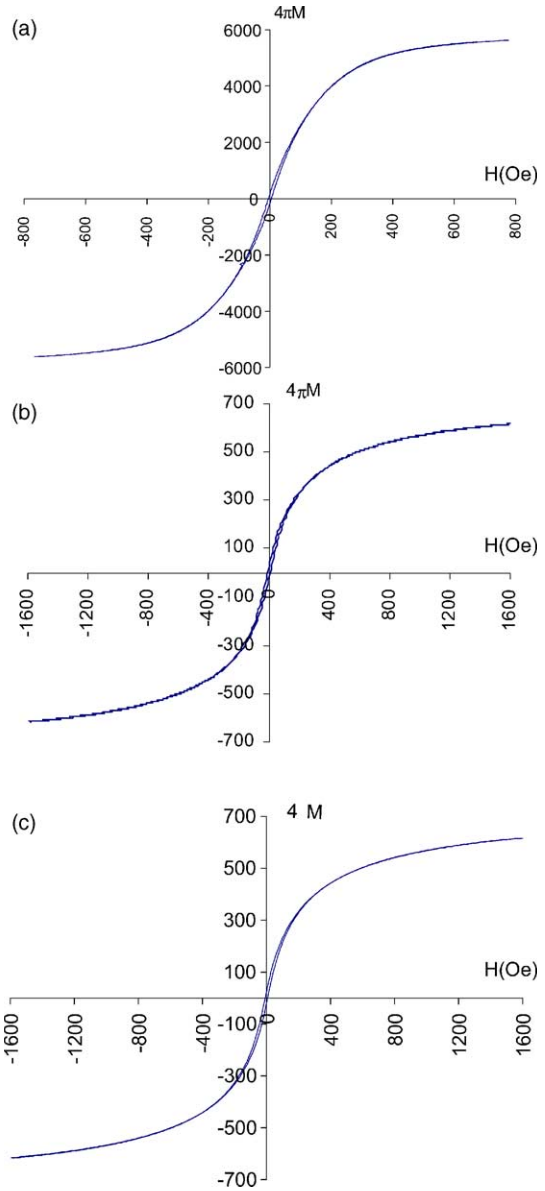

Fig. 5. Hysteresis loops for (a) Fe_3Si powder, (b) HVOF coatings and (c) APS coatings.

4. Calculation details

4.1. Method

Our calculations were carried using the full potential linear augmented plane wave (FPLAPW), a first-principle total energy density functional theory (DFT)-based method. We used the scalar relativistic version without spin orbit coupling [16] as embodied in the WIEN2k code [17] which is thought to be from the most accurate implementations of the FPLAPW methods for the computation of the electronic structure of solids within density functional theory. In the FPLAPW method, the crystal unit cell is divided into two parts: atomic spheres centered on the atomic sites and an interstitial region. Inside the atomic spheres, the basis set used to describe electronic states employs atomic like functions, while in the interstitial region plane waves are used. Exchange and correlation effects were treated using the generalized gradient approximation (GGA) as described by Perdew and coworkers [18,19].

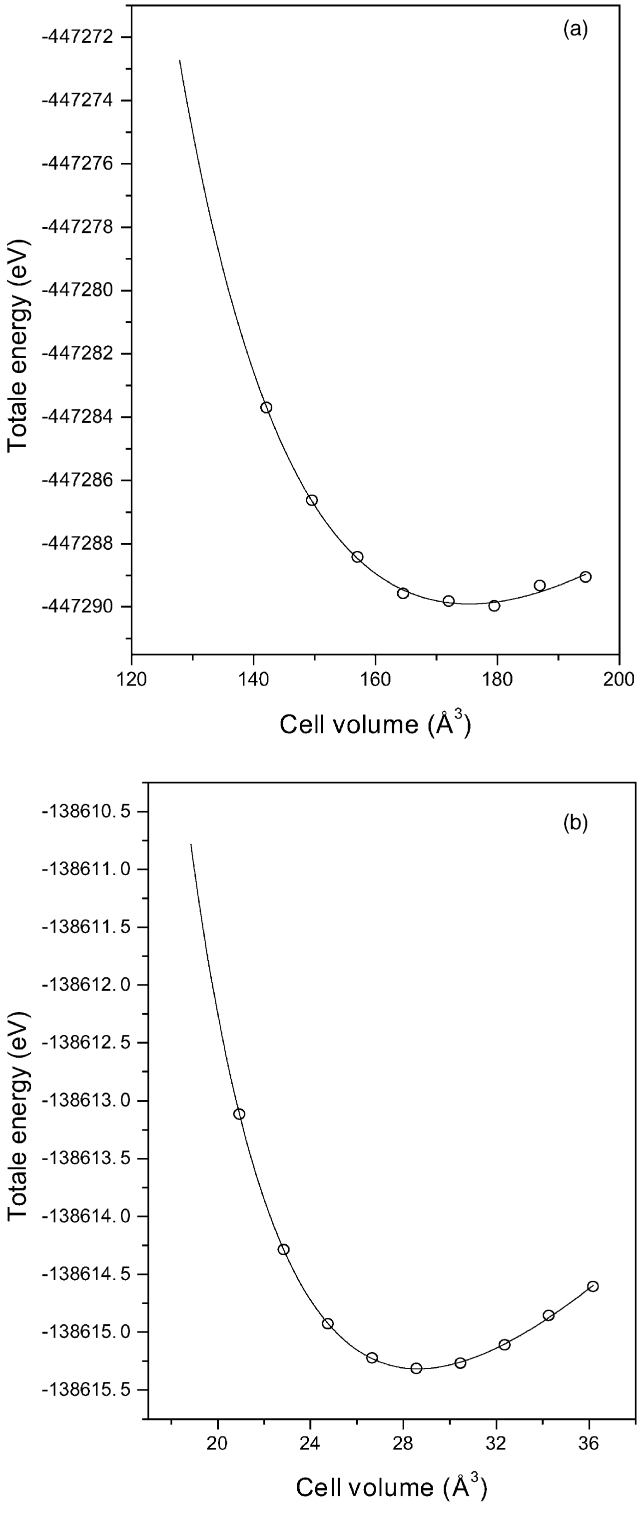

Fig. 6. Total energy vs. volume change for (a) cubic Fe_3Si and (b) rhombohedral FeNb fitted to the Murnaghan equation of state.

4.2. Structure optimization

Following the XRD results, Fe_3Si forms a cubic structure in the *Im*3*m* (2 2 9) space group, whereas FeNb crystallizes in the rhombohedral *R*-3*m* (1 6 6) structure. Accordingly, we first undertake the structural optimization of both materials. The total energy was calculated self-consistently for different volumes, leading to the energy versus volume plot that we fit to the Murnaghan equation of state [20] to obtain the equilibrium volume, total energy and bulk modulus. In all calculations a set of 200–30,000 points where used in the irreducible Brillouin zone (IBZ), and the self-consistent cycles where terminated when both the energy and the charge density reaches an accuracy of 10^{-5}. In the case of FeNb, the *c*/*a* ratio was first optimized following the same method, but fitting the energy versus *c*/*a* ratio-resulting curves to a second-order polynomial equation. Fig. 6a and b shows the total energy versus volume change for cubic Fe_3Si and rhombohedral FeNb. Table 2 reports the equilibrium calculated lattice parameters, total energies and bulk modulus for both materials.

Our interest being on the influence of boron impurities in the Fe_3Si lattice on its electronic properties, first we have to find the new lattice parameters after the introduction of boron atoms in the structure. For that we have used the suppercell method: we reduced the symmetry of the lattice by making equivalent positions nonequivalent, we created a translational reproductions of the unit cell, then we removed at each time an iron atom and replaced it by a boron one. Hence, we created doped structures with 8, 16 and 25 at.% of boron. For the Brillouin zone sampling we followed the rule of thumb that stipulates that the size of the *k*-mesh for the suppercell must be that of the unit cell (original one) multiplied by the ratio of the volumes of simulation cells. This, with the fact that the computational time grow rapidly with growing *k*-mesh, we were not able to simulate smaller amounts of boron. As before, we plotted the energy versus volume and fitted to the Murnaghan equation of state. The resultant structural properties are presented in Table 2.

Table 2
Calculated equilibrium volume and bulk modulus for FeNb, Fe_3Si and B-doped Fe_3Si compounds

Material	Equilibrium volume ($Å^3$)	Bulk modulus (Gpa)
FeNb	28.63	177.97
Fe_3Si	175.32	183.61
Fe_3Si–8 at.% B	167.42	195.21
Fe_3Si–16 at.% B	160.61	235.40
Fe_3Si–25 at.% B	154.81	252.25

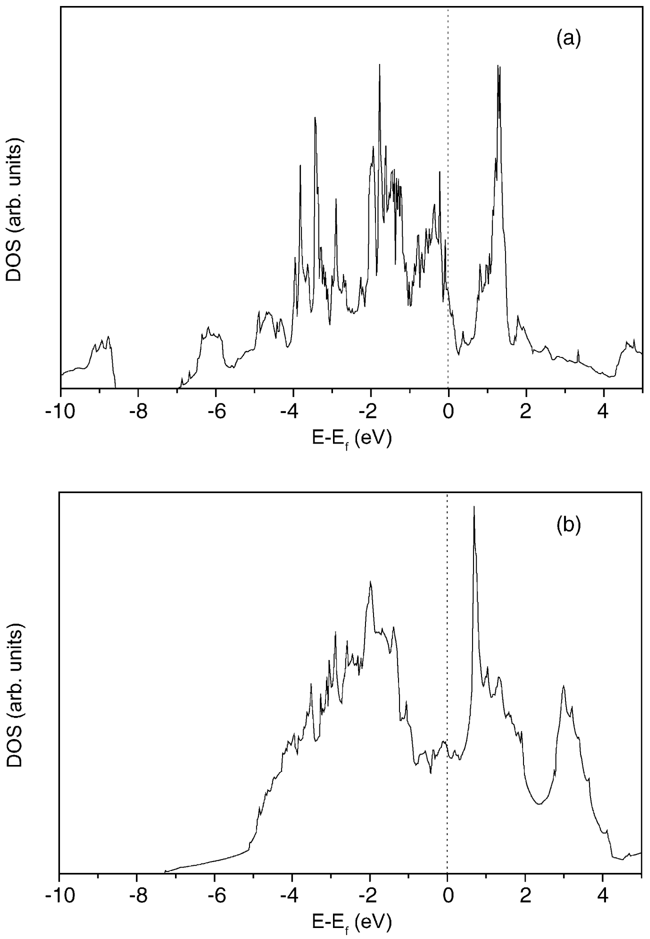

Fig. 7. Electronic density of state of (a) Fe_3Si and (b) FeNb.

4.3. Electronic structure

Once the crystal structures optimized, we focus on the electronic properties. We run the self-consistent cycle for each structure, then the electronic density of state (DOS) was calculated using the modified tetrahedron method of Blöchl et al. [21]. Fig. 7 shows the electronic density of state of both alloys (zero represents the Fermi level). The DOS histograms show the bonding state orbitals near the Fermi level and the top of the density curve with the antibonding states. The major difference that we can assert is the presence in the Fe_3Si histogram of a minimum of density just beyond the Fermi level, separating the peak of the antibonding states, whereas for FeNb the Fermi level is directly followed by a pronounced peak. In both compounds, the antibonding states are the localized d states: 4d-states from iron atoms in both cases, and 3d-states from niobium atoms in the second. Another difference is that the peak of the lower energy part of the DOS present for Fe_3Si and which is due mainly to the tightly bounded s states, is not visibly separated from the remaining parts of the DOS for the FeNb alloy. Accordingly, at finite temperatures, the antibonding states are much more populated in the case of FeNb alloy. The minimum of density beyond the Fermi level separating the bonding from the antibonding states in the iron silicon alloy denotes its structural stability.

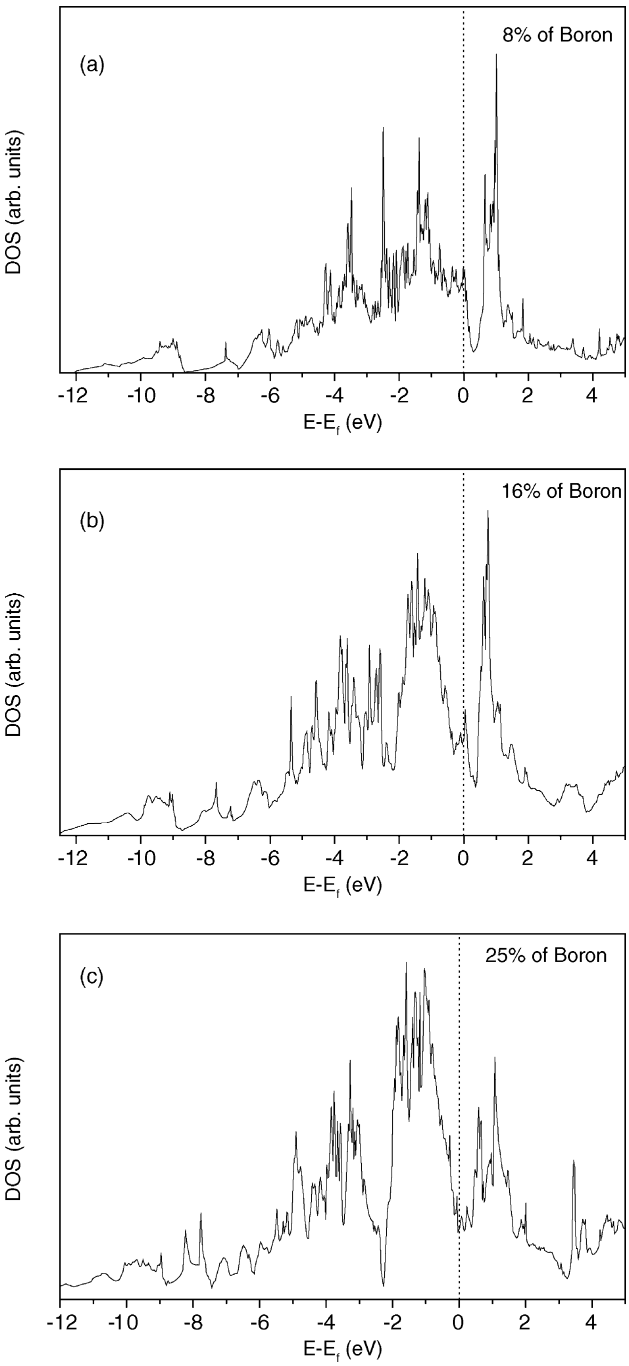

Fig. 8. (a)–(c) Electronic density of state of boron-doped Fe_3Si alloy.

The density of state of B-doped Fe_3Si is shown in Fig. 8a–c. We notice that the shape of DOS histogram is different: the addition of boron atoms annihilate gradually the minimum present near the Fermi level. In fact, we see that this minimum is slightly reduced when the boron concentration is of 4 at.%, and is less pronounced for 16 at.% and disappears for 25 at.% of boron. At the same time, we note that the peak present in the bonding state is progressively

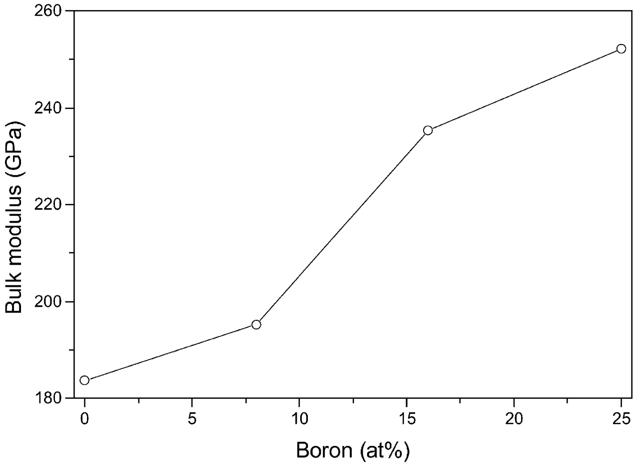

Fig. 9. Variation of bulk modulus values with boron content.

pronounced, especially, at the Fermi level the density grows with increasing boron concentration. This is in conformity with the calculated values of bulk modulus. In fact, this later increases with the amount of boron, as shown in Fig. 9.

The fact that the antibonding states are more populated suggests that the addition of boron weaken the crystalline structure stability, even it reinforce the bonds as stated by the increasing bulk modulus. Furthermore, the lowest energy states are progressively connected with the remainder part of the histogram. Both changes make the electronic density of state to be similar to the FeNb one. Therefore, the bonding nature in the Fe_3Si tends to have the same behavior than that of FeNb owing to the presence of boron.

5. Conclusions

This work is a preliminary contribution to the iron-based thermally sprayed coatings intended for magnetic applications. The following conclusions can be drawn:

1. A combination of experimental and numerical studies on deposits obtained by HVOF and APS thermal spraying of Fe_3Si and FeNb alloys has allowed to compare the $Fe_3Si(B)$ and FeNb structures. Contrary to the cases of the microcrystalline Fe_3Si deposits, thermally sprayed FeNb made it possible to obtain coatings with a partially amorphous structure.
2. Boron atoms were used to improve the aptitude of the Fe_3Si alloy to form an amorphous phase. In this perspective, first-principle calculations were elaborated to investigate the electronic structure of crystalline FeNb and Fe_3Si. It has been shown that the introduction of boron impurities into the alloy matrix leads to the lowering of the structural stability, and makes its electronic density of state more comparable to the one corresponding to the niobium-iron structure.
3. Experimental results have shown clearly that FeNb alloys can be easily obtained in an amorphous state. According to the results obtained, and since the crystalline structure stability is intimately bound to the electronic structure properties, the addition of boron in the Fe_3Si alloy matrix will improve its amorphization ability.

References

[1] J.C. Perron, Constantes Physico-Chimiques, Techniques de l'Ingénieur, vol. K4, Imprimerie Strasbourgeoise, Schiltigheim, France, 1994.

[2] F.E. Luborsky, Amorphous Metallic Alloys, Butterworths, London, 1983.

[3] R.C. O'Handley, J. Megusar, S.W. Sun, Y. Hara, N.J. Grant, J. Appl. Phys. 57 (1985) 3563.

[4] A. Borisova, Y. Borisov, V. Korzhyk, V. Bobrik, in: Proceedings of the ITSC'95, Kobe, May 1995, p. 749.

[5] M. Nakayama, H. Ito, R. Nakamura, M. Toh, A. Ohmori, in: Proceedings of the ITSC'95, Kobe, May 1995, p. 1063.

[6] H. Herman, S. Sampath, in: Proceedings of the Second Plasma Technik Symposium, Lucerne, Switzerland, 1991, p. 63.

[7] G. Föoex, J. Phys. Radium 9 (1938) 37.

[8] R. Benoit, J. Chim. Phys. 52 (1955) 119.

[9] J.C. Swartz, R. Kossowsky, J.J. Haugh, R.F. Krause, J. Appl. Phys. 52 (1981) 3324.

[10] T.V. Larionova, O.V. Tolochko, A.S. Zhuravley, Glass Phys. Chem. 21 (1995) 297.

[11] T.V. Larionova, O.V. Tolochko, N.O. Gonchukova, E.V. Novikov, Glass Phys. Chem. 22 (1996) 248.

[12] N.E. Fenineche, M. Cherigui, A. Kellou, H. Aourag, C. Coddet, in: Proceedings of the Thermal Spray, ASA, Orlando, 2003, p. 1409.

[13] G.K. Wertheim, V. Jaccarino, J.H. Wernick, J.A. Seitchik, H.J. Williams, R.C. Sherwood, Phys. Lett. 18 (1965) 89.

[14] L.K. Varga, F. Mazaleyrat, J. Kovac, A. Kàkay, Mater. Sci. Eng. A 304–306 (2001) 946.

[15] M. Abdellaoui, C. Djega-Mariadassou, E. Gaffet, J. Alloys Compd. 259 (1997) 241.

[16] D.D. Koelling, B.N. Harmon, J. Phys. Solid State Phys. 10 (1977) 3107.

[17] P. Blaha, K. Schwarz, G.K.H. Madsen, D. Kvasnicka, J. Luitz, WIEN2k, An Augmented Plane Wave + Local Orbitals Program for Calculating Crystal Properties, Vienna University of Technology, Austria, 2001.

[18] J.P. Perdew, J.A. Chevary, S.H. Vosko, K.A. Jackson, M.R. Pederson, D.J. Singh, C. Fiolhais, Phys. Rev. B 46 (1992) 6671.

[19] J.P. Perdew, Y. Wang, Phys. Rev. B 45 (1992) 13244.

[20] F.D. Murnaghan, Proc. Nat. Acad. Sci. U.S.A. 30 (1944) 244.

[21] P.E. Blöchl, O. Jepsen, O.K. Andersen, Phys. Rev. B 49 (1994) 16223.